Anomalous photoelectron angular distribution in ionization of Kr in intense ultraviolet laser fields

Motoyoshi Nakano,[1] Tomohito Otobe,[2] and Ryuji Itakura[2,*]

[1]*Department of Chemistry, Graduate School of Science, Tohoku University, Aoba-ku, Sendai 980-8578, Japan*

[2]*Kansai Photon Science Institute, National Institutes for Quantum and Radiological Science and Technology (QST), 8-1-7 Umemidai, Kizugawa, Kyoto 619-0215, Japan*

(Received 8 March 2017; published 5 June 2017)

We investigate multiphoton ionization of Kr for the formation of the two spin-orbit split states $^2P_{1/2}$ and $^2P_{3/2}$ of Kr^+ in intense ultraviolet femtosecond laser fields ($\lambda \approx 398$ nm, $\tau \approx 50$ fs). As the laser intensity increases from 8 to 39 TW cm^{-2}, the photoelectron angular distribution (PAD) exhibits the anomalous enhancement in the direction perpendicular to the laser polarization. With the support of the time-dependent density functional theory taking account of the spin-orbit interaction, the measured anomalous PAD is ascribed to the autoionization to $^2P_{3/2}$.

DOI: 10.1103/PhysRevA.95.063404

I. INTRODUCTION

Ionization of atoms and molecules in intense laser fields has been investigated since the invention of the laser. The measured ionization yields of rare gases as a function of the laser intensity were reproduced by the calculation based on the theory, taking account of the interaction between the initial bound state and the final continuum [1–5]. By measuring photoelectron spectra for more details, above threshold ionization (ATI) was discovered as a unique feature in strong field ionization [6].

As the intensity of femtosecond laser pulses varied, the presence of resonant Rydberg states was identified in photoelectron spectra at a specific laser intensity, indicating that the ponderomotive energy shift brings Rydberg states into multiphoton resonance [7,8]. Unlike the nonresonant ionization, the resonant ionization shows no energy shift as a function of the laser intensity, because the ionization continuum and the highly lying Rydberg levels are similarly shifted by the ponderomotive energy.

Photoelectron angular distributions (PADs) of rare gas atoms were also investigated as a function of laser wavelength and intensity [9–13]. It was revealed that the orbital angular momentum l of photoelectrons increases by $\Delta l = +1$ from l of resonant Rydberg levels, from which one-photon ionization takes place. Regarding ATI, the orbital angular momentum l of photoelectrons increases by $\Delta l = +1$ with an increase of one photon in the absorbed photon number irrespective of the presence of a resonant intermediate state.

In addition to the resonant intermediate states, it was also revealed that photoemission from an inner valence orbital is induced by intense laser fields, resulting in the formation of ions in electronically excited states [14–18]. Furthermore, the coherent superposition of the spin-orbit split states $^2P_{3/2}$ and $^2P_{1/2}$ of rare gas ions was experimentally confirmed through the quantum beat measurement [19–24] and theoretically described [25–28]. Thus, multiple electronic states of both neutral and ionic levels make significant contributions in ionization in intense laser fields.

Recently, intermediate states in strong field ionization have been investigated intensively [29–34]. In ionization induced by an attosecond pulse, the electronic dynamics prior to photoemission can be controlled by dressing a couple of states using an intense laser pulse [35–40]. If ionization is induced by a single intense laser pulse, the laser pulse has to play two roles in dressed state formation and in photoemission, simultaneously. Such coupling mechanisms among electronic bound states and continua still have plenty of room for further investigation.

In the present study, we investigate ionization of Kr for the formation of the two spin-orbit split states of $Kr^+(4p^{-1})$, $^2P_{1/2}$ and $^2P_{3/2}$, in intense UV femtosecond laser fields. We have measured three-dimensional (3D) photoelectron momentum distributions as a function of laser peak intensity I_0. It has been found that photoelectrons are emitted dominantly in the direction perpendicular to the laser polarization direction at the laser peak intensity of $I_0 = 39$ TW cm^{-2} (TW $= 10^{12}$ W). For discussion on the ionization mechanism causing anomalous PADs, we have performed an *ab initio* calculation based on the time-dependent density functional theory (TDDFT) in which the relativistic effect causing the spin-orbit splitting is taken into account. Indeed, the calculation of the spin-orbit interaction in intense laser fields is a theoretical challenge.

II. EXPERIMENTAL

Details of the experimental setup used in this study were described in previous publications [41,42]. Briefly, linearly polarized UV femtosecond pulses [$\lambda \approx 398$ nm, $\tau \approx 50$ fs (FWHM), 1 kHz] were obtained by frequency doubling of output pulses from a Ti:sapphire chirped-pulse regenerative amplification system. The temporal wave form of the UV pulses was characterized by self-diffraction frequency-resolved optical gating [43]. The UV pulses were focused on a pure Kr beam, which was introduced into an ultrahigh vacuum chamber through a microsyringe as a skimmed effusive beam. The background pressure in the chamber was below 10^{-8} Pa. The flow rate of the sample gas was controlled with a variable leak valve (Varian) so that the detection count rate was smaller than 0.8 events per laser shot.

By using a fast microchannel plate detector with a position-sensitive delay-line anode (RoentDek HEX80), the 3D momentum vector of each photoelectron was measured in a single-shot acquisition mode. In order to reduce the position

*itakura.ryuji@qst.go.jp

dependence of the detection efficiency, the PADs $P(\theta)$ with inversion symmetry were obtained from the raw data of the PADs $P_{\rm raw}(\theta)$ as

$$P(\theta) = P(180^\circ - \theta) = \frac{P_{\rm raw}(\theta) + P_{\rm raw}(180^\circ - \theta)}{2}, \quad (1)$$

where θ is the polar angle with respect to the laser polarization direction ($\theta = 0$ and 180°).

The measurements were carried out at different laser peak intensities in the range of $I_0 = 8$–39 TW cm^{-2}. The laser peak intensities I_0 at the focal spot were estimated from the ponderomotive energy shift ($U_{\rm p}$) [7] in the photoelectron spectra.

III. THEORETICAL METHOD

The electronic dynamics in intense laser fields can be described with the TDDFT [44]. A time-dependent N-electron system was solved with two-component electronic wave functions $\psi_i(\vec{r},t) = (\psi_{i,\alpha}(\vec{r},t), \psi_{i,\beta}(\vec{r},t))$ satisfying the time-dependent Kohn-Sham equation,

$$i\hbar\frac{\partial}{\partial t}\psi_i(\vec{r},t) = \Bigg[-\frac{\hbar^2}{2m}\nabla^2 + V_{\rm H}[\rho(\vec{r},t)] + V_{\rm xc}[\rho_\alpha(\vec{r},t),\rho_\beta(\vec{r},t)] + \hat{V}_{\rm ion} + \mu_B\vec{\sigma}\cdot\vec{B}_{\rm xc} + \hat{V}_{\rm SO} - e\vec{r}\cdot\vec{E}_{\rm ext}(t)\Bigg]\psi_i(\vec{r},t), \quad (2)$$

where $\rho_{\alpha(\beta)}(\vec{r},t) = \sum_i |\psi_{i,\alpha(\beta)}(\vec{r},t)|^2$ and $\rho(\vec{r},t) = \rho_\alpha(\vec{r},t) + \rho_\beta(\vec{r},t)$ are the electron densities, $V_{\rm H}$ the Hartree potential, $V_{\rm xc}$ and $\vec{B}_{\rm xc}$ the spin-independent and dependent exchange-correlation potential, respectively, $\hat{V}_{\rm ion}$ the potential of the ion, $\hat{V}_{\rm SO}$ the spin-orbit interaction, and $E_{\rm ext}(t)$ the external laser field, which is linearly polarized. We employed a conventional noncollinear local spin density approximation (NC-LSDA) [45,46] as the exchange-correlation potentials of $V_{\rm xc}$ and $\vec{B}_{\rm xc}$. The Hartwigsen-Goedecker-Hutter (HGH) pseudopotential, including the spin-orbit interaction, was used for $\hat{V}_{\rm ion}$ and $\hat{V}_{\rm SO}$ [47]. In this calculation, the magnetic field of the laser pulse was neglected and the system was spin unpolarized.

The time-dependent Kohn-Sham equation [Eq. (2)] was solved numerically by a grid-based method in real-space [48]. The time propagation of the Kohn-Sham orbitals was carried out by using a fourth-order Taylor expansion, and the Laplacian operator was evaluated by the nine-point difference formula. We took a constant time step of 0.000 66 fs and utilized uniform grids in the 3D Cartesian coordinate with a mesh spacing of 0.2 Å. The total number of the time steps was 100 000. We carried out the numerical calculations employing grid points inside a spherical box whose radius was $R = 40$ Å. To absorb the emitted electron, we adopted an absorbing potential $W(r)$ with a linear dependence on the coordinate r as [49]

$$W(r) = \begin{cases} 0 & (0 < r < R) \\ -iW_0\frac{r-R}{\Delta r} & (R < r < R + \Delta r). \end{cases} \quad (3)$$

We set the height W_0 and width Δr to be 10 eV and 10 Å, respectively.

The ionization potentials (IPs) of Kr for the formation of the two spin-orbit levels $^2P_{3/2}$ and $^2P_{1/2}$ of $Kr^+(4p^{-1})$ were calculated to be 9.3 and 10.3 eV, respectively, while the measured IPs of Kr are 13.999 6 eV for $^2P_{3/2}$ and 14.665 4 eV for $^2P_{1/2}$ [50]. The discrepancy in the IP from the measurement is a well-known problem originating from (i) the spurious self-interaction energy in the LSDA and (ii) the incorrect long-range potential deviated from the Coulomb potential [51]. Nevertheless, comparisons between the experimental and calculated results are meaningful within the framework of the nonresonant multiphoton ionization. In the calculation, we reduced the laser frequency such that the minimum photon number required for the ionization is the same as that in the experiment.

Since the Keldysh parameter γ is a good measure for evaluating whether the ionization mechanism is multiphoton or tunneling [2,52], the laser intensity I_0 in the calculation was also set so that the γ values are similar to the experiment. When we calculated γ, the calculated IPs, 9.3 and 10.3 eV for $^2P_{3/2}$ and $^2P_{1/2}$, respectively, were used for self-consistency. As I_0 increases from 8 to 39 TW cm^{-2} in the experiment with $\hbar\omega = 3.1$ eV ($\lambda = 398$ nm), the Keldysh parameter decreases from $\gamma = 7.7$–3.5 for the $^2P_{3/2}$ channel. The Keldysh parameter of $\gamma > 1$ at $I_0 = 39$ TW cm^{-2} suggests that the multiphoton ionization mechanism is dominant even at the highest intensity in the present experiment. We set the laser frequency in the calculation to be $\hbar\omega = 2.1$ eV, with which the dominant ionization process proceeds by the five-photon absorption for the calculated IPs.

We adopted a quasi-CW laser field,

$$E_{\rm ext}(t) = \begin{cases} E_0 \sin^2\pi\frac{t}{2T}\sin\omega t & (0 < t < T) \\ E_0 \sin\omega t & (T < t), \end{cases} \quad (4)$$

where T is set to be 5 fs. The amplitude of the laser electric field E_0 is obtained from the equation of $I_0 = \epsilon_0 c {E_0}^2/2$. Although the laser wave form described by Eq. (4) is different from that in the experiment, this type of wave form is frequently used to secure the computational accuracy [53]. Since the ionization probability depends on the laser intensity exponentially, ionization takes place dominantly when the amplitude of the laser field is the maximum. The ionization yields in the rising and falling regions of the pulse are negligible. Since the laser pulse duration of 50 fs (FWHM) in the present experiment is much longer than an optical cycle of 1.3 fs, the temporal variation of the laser field amplitude is sufficiently slow and the temporal region around the peak can be regarded as a quasi-CW electric field. It is true that the laser wave form in the calculation is different from the actual wave form, but the quasi-CW field used in this study is sufficiently relevant to describe nonresonant multiphoton ionization. In order to obtain the ionization probability sufficiently larger than the accumulated computational error, the relatively long CW field was applied. The smooth ramping at the beginning of the laser field was also applied to avoid artificial nonadiabatic excitation and ionization. The number of emitted electrons was counted in the respective ionization channels, $^2P_{3/2}$ and $^2P_{1/2}$, at the boundary ($r = R$). The counted numbers of the electrons as a function of the emission angle θ were divided by $\sin\theta$ to obtain the calculated PADs.

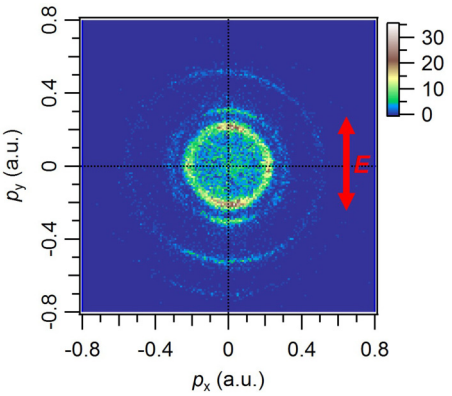

FIG. 1. Two-dimensional sliced image of the 3D momentum distribution of photoelectrons emitted from Kr at the laser peak intensity of $I_0 = 18$ TW cm^{-2}. The photon energy is 3.1 eV (398 nm) and the laser polarization direction is along the vertical (y) axis. The unit of the coordinates is the atomic unit (a.u.).

IV. RESULTS AND DISCUSSION

A. Photoelectron momentum distribution

The energy of no less than five photons ($5\,\hbar\omega = 15.5$ eV) is required to form both two spin-orbit levels $^2P_{3/2}$ and $^2P_{1/2}$ of Kr^+ in the electronic ground state from the neutral Kr in the electronic ground state [50]. Figure 1 shows the 2D sliced image of the 3D momentum distribution of photoelectrons measured at $I_0 = 18$ TW cm^{-2}. This image was obtained by extracting the data in the range of $|p_z| < 0.02$ atomic units (a.u.) from the 3D distribution of the photoelectron momentum, where p_z stands for the momentum component along the time-of-flight tube axis and perpendicular to the detector plane. The photoelectron spectra and angular distributions were obtained from the sliced images. We confirmed the slicing thickness of $|p_z| < 0.02$ a.u. was sufficiently thin for the photoelectron spectra and angular distributions to be correctly extracted. Multiphoton ionization of Kr to the two spin-orbit states $^2P_{3/2}$ and $^2P_{1/2}$ appears as concentric rings. The rings at the momenta of 0.2 and 0.3 a.u. correspond to the five-photon ionization of Kr to Kr^+ $^2P_{1/2}$ and $^2P_{3/2}$ states, respectively. The ring at the momentum of 0.5 a.u. corresponds to ATI resulting from the six-photon absorption of Kr.

Figures 2(a)–2(c) indicate the photoelectron spectra at $I_0 = 8$,18, and 39 TW cm^{-2}, respectively. The two peaks in the energy range of 0–2 eV are assigned to the five-photon ionization for the formation of Kr^+ $^2P_{1/2}$ and $^2P_{3/2}$ from the lower energy side. The results of the least-squares fitting of Lorentzian functions to the measured photoelectron spectra in the energy range of 0–2 eV are shown in Fig. 2. The peaks of the six- and seven-photon ATI are also recognized in the energy ranges of 3–5 eV and 6 – 8 eV, respectively, as minor peaks.

B. Photoelectron angular distributions

1. Five-photon ionization

For the respective ionization channels of Kr to Kr^+ $^2P_{3/2}$ and $^2P_{1/2}$, PADs were extracted. The separation of these two channels was based on the photoelectron energy. At $I_0 = 8$ TW cm^{-2}, the photoelectrons in the energy ranges

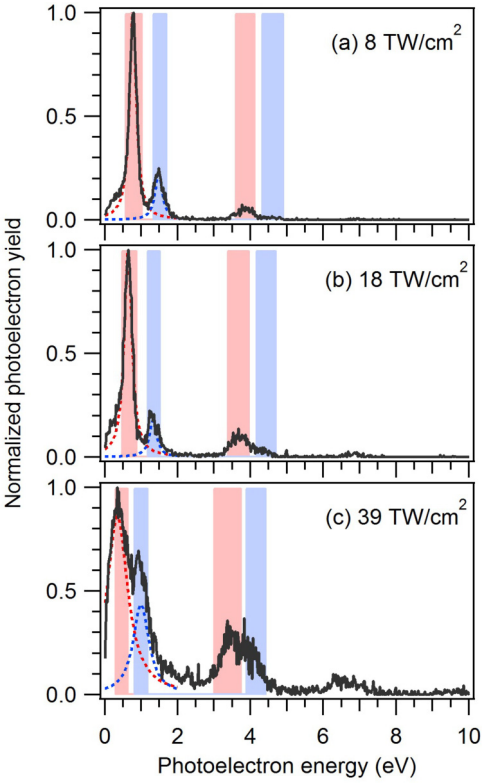

FIG. 2. Measured photoelectron spectra of Kr at the laser peak intensities of $I_0 =$ (a) 8, (b) 18, and (c) 39 TW cm^{-2} (solid curves). The photon energy is 3.1 eV (398 nm). The results of the least-squares fitting of the two peaks assigned to the five-photon ionization to $^2P_{1/2}$ and $^2P_{3/2}$ are represented by dotted curves. Photoelectrons falling in the hatched energy ranges are counted in constructing photoelectron angular distributions for the five-photon ionization of Kr to Kr^+ $^2P_{1/2}$ and $^2P_{3/2}$, and for the six-photon ionization to Kr^+ $^2P_{1/2}$ and $^2P_{3/2}$, respectively, from the lower energy side.

of 1.308–1.667 eV and 0.544–0.992 eV were counted for the five-photon ionization channels to the formation of Kr^+ $^2P_{3/2}$ and $^2P_{1/2}$, respectively. As I_0 increases, each peak energy is shifted by the ponderomotive energy as shown in Fig. 2. At $I_0 = 39$ TW cm^{-2}, the photoelectrons in the energy ranges of 0.784–1.144 eV and 0.267–0.600 eV were counted for the five-photon ionization channels to the formation of Kr^+ $^2P_{3/2}$ and $^2P_{1/2}$, respectively. The PADs of the five-photon ionization channels to the formation of Kr^+ $^2P_{3/2}$ and $^2P_{1/2}$ at $I_0 = 8$, 18, and 39 TW cm^{-2} are plotted in Figs. 3(a)–3(c), respectively. The Keldysh parameters are $\gamma = 7.7$, 5.1, and 3.5 for the ionization to $^2P_{3/2}$, and $\gamma = 7.9$, 5.3, and 3.6 for the ionization to $^2P_{1/2}$ at $I_0 = 8$, 18, and 39 TW cm^{-2}, respectively. Although the two peaks are overlapped at the highest intensity of $I_0 = 39$ TW cm^{-2}, the remarkable difference between the PADs of the two channels can be recognized as shown in Fig. 3(c).

At $I_0 = 8$ TW cm^{-2}, photoelectrons are emitted dominantly along the laser polarization direction and partly in the direction perpendicular to the laser polarization. In the $^2P_{3/2}$ channel, the PAD exhibits a substantial yield in the range of $\theta = 45^\circ - 135^\circ$. The angular range of photoelectron emission toward the perpendicular direction ($\theta = 90^\circ$) in the $^2P_{1/2}$

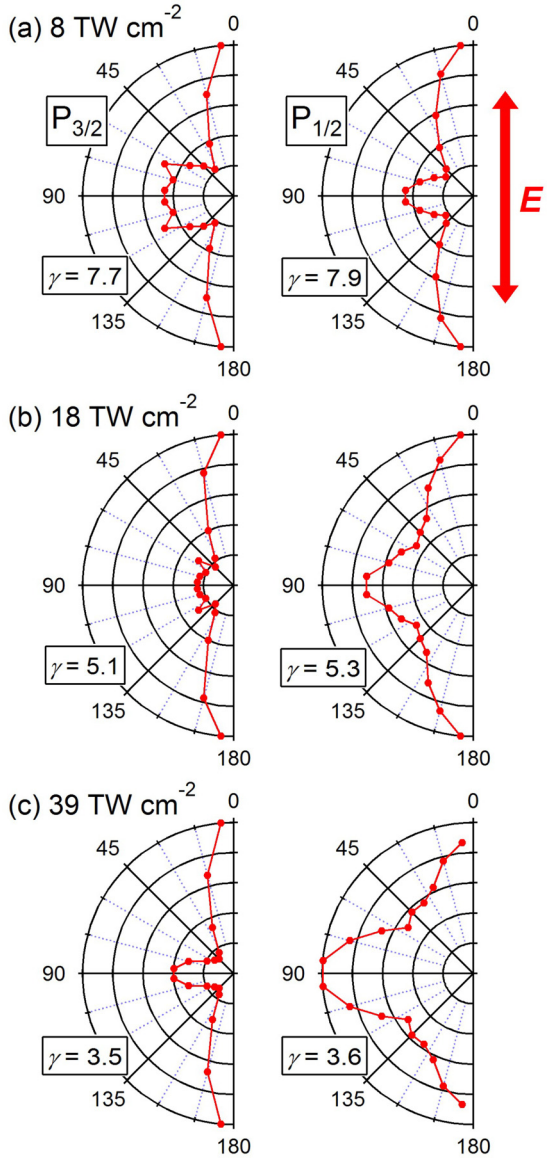

FIG. 3. Polar plots of measured photoelectron angular distributions in the energy ranges of the photoelectrons assigned to the five-photon ionization of Kr to Kr^+ $^2P_{3/2}$ (left) and $^2P_{1/2}$ (right) at the laser peak intensities I_0 = (a) 8, (b) 18, and (c) 39 TW cm^{-2}. The photon energy is 3.1 eV (398 nm) and the laser polarization direction is vertical ($\theta = 0$ and 180°), as indicated by a double-headed arrow in the top right.

channel is narrower than that in the $^2P_{3/2}$ channel. Compared to $I_0 = 8$ TW cm^{-2}, the photoemission toward $\theta = 90°$ in the $^2P_{3/2}$ channel is suppressed at $I_0 = 18$ TW cm^{-2}, and meanwhile, it is recovered at $I_0 = 39$ TW cm^{-2}, with a narrower angular distribution. On the other hand, in the $^2P_{1/2}$ channel, the photoemission in the direction perpendicular to the laser polarization direction is anomalously enhanced with increasing I_0 from 8 to 39 TW cm^{-2}. In strong field ionization, photoelectrons tend to be dominantly emitted in the direction along the laser polarization. It is anomalous that the photoemission yield in the direction perpendicular to the laser polarization is larger than that in the direction along the laser polarization.

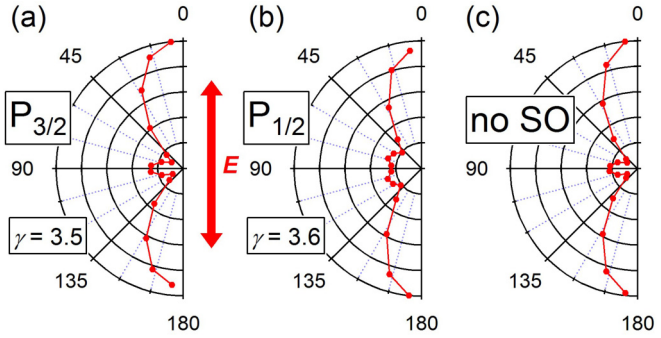

FIG. 4. Polar plots of calculated PADs for the ionization of Kr to Kr^+ (a) $^2P_{3/2}$ and (b) $^2P_{1/2}$ at the laser peak intensity $I_0 =$ 12 TW cm^{-2} corresponding to the Keldysh parameters $\gamma = 3.5$ and 3.6, respectively. The photon energy is 2.1 eV and the laser polarization direction is vertical. For comparison, the calculated PAD without taking spin-orbit interaction into account is also plotted in (c).

The PADs were theoretically calculated at the Keldysh parameters $\gamma = 3.5$ [Fig. 4(a)] for the ionization of Kr ^1S to Kr^+ $^2P_{3/2}$, and $\gamma = 3.6$ [Fig. 4(b)] for the ionization to $^2P_{1/2}$, where the laser intensity was set to be $I_0 = 12$ TW cm^{-2}. The calculated ionization probabilities are 1 or 2 orders of magnitude larger than the accumulated computational error at this laser intensity, while the ionization probability becomes comparable to the error as the laser intensity decreases. Therefore we compare the calculated results with the experimental results only at the smallest Keldysh parameters, that is, the highest laser intensity.

The calculated PAD in the $^2P_{3/2}$ channel [Fig. 4(a)] exhibits the main peaks at around $\theta = 0°$ and 180°, which are parallel to the laser polarization direction ($\theta = 0°$ and 180°). The small yield of the perpendicular emission in the angular range of $\theta = 70°$–$110°$ is also seen. This PAD is close to the d_0 orbital ($l = 2, m_l = 0$), where l and m_l are the orbital angular momentum and its magnetic quantum number, respectively, and qualitative agreement with the experimentally measured PAD is obtained. In the $^2P_{1/2}$ channel, the calculated PAD [Fig. 4(b)] exhibits dominant peaks at $\theta = 0°$ and 180°, with minor peaks at $\theta = 70°$ and 110°. The significantly enhanced photoemission yield in the direction of $\theta = 90°$ is not reproduced in the calculated PAD, which has a major contribution of larger l photoelectron orbitals such as an f_0 orbital ($l = 3, m_l = 0$) and/or photoelectron orbitals with $m_l = 1$ such as a d_1 orbital. All photoemission events with different numbers of absorbed photons were counted in the calculation. The five-photon ionization is considered to be dominant, but the six-photon ionization is also included as a minor contribution.

In order to clarify the role of the spin-orbit interaction, we calculated the PAD without taking the spin-orbit interaction into account. As shown in Fig. 4(c), the PAD is quite similar to the d_0 orbital. When the spin-orbit interaction is included, the calculated PAD in the $^2P_{3/2}$ channel is almost the same as the PAD with no spin-orbit interaction. A slight influence by the spin-orbit interaction appears in the calculated PAD in the $^2P_{1/2}$ channel in the angular range of $\theta = 60$–$120°$.

Contrary to calculated PADs where the photoemission along the laser polarization direction is dominant, the

experimentally measured PADs in the $^2P_{1/2}$ channel indicate the anomalous enhancement of the photoemission perpendicular to the laser polarization direction. The slight influence by the spin-orbit interaction in the calculation cannot account for the anomalous enhancement of the photoemission toward $\theta = 90^\circ$. This discrepancy suggests that one or more important processes in the course of the ionization are not included in the theoretical framework.

In the previous studies, it was reported that autoionizing states of Kr below the ionization threshold for the formation of $Kr^+ {}^2P_{1/2}$ exhibit the photoemission in the direction perpendicular to the laser polarization direction [54,55]. Using a nanosecond dye laser [54] or a synchrotron light source [55], the anisotropy parameter β of the photoemission from the ns' autoionizing states of Kr was measured to be negative, indicating that the photoemission in the direction perpendicular to the laser polarization direction is preferred.

Although the autoionization forms $Kr^+ {}^2P_{3/2}$, the photoelectron energy in the autoionization might coincide with that in the nonresonant five-photon ionization for the formation of the other state $^2P_{1/2}$ in intense laser fields. The photoelectron energy in the nonresonant ionization is shifted toward the lower energy by the ponderomotive energy U_p (eV) $= 1.4794\, I_0 \times 10^{-2}$ at $\lambda = 398$ nm, where I_0 is in the unit of TW cm^{-2}. On the other hand, the photoelectron energy resulting from the autoionization hardly changes with increasing I_0, because the lifetime of the autoionizing states is much longer than the femtosecond laser pulse duration. The photoemission takes place mostly after the laser pulse is gone. Even if the photoemission in the autoionization takes place within the laser pulse duration, the ponderomotive energy shift of the autoionizing levels with a highly lying Rydberg electron is as large as that of the ionization threshold, resulting in no energy shift of the photoelectron from the autoionizing levels. The photoelectron energy from the autoionizing level of Kr $10s'$ to $Kr^+ {}^2P_{3/2}$ with the perpendicular photoemission is known to be around 0.35 eV [50], which accidentally coincides with the photoelectron energy of the nonresonant ionization of Kr to $Kr^+ {}^2P_{1/2}$ shifted by the ponderomotive energy at $I_0 = 39$ TW cm^{-2}. Therefore, it is probable that the autoionization of Kr to form $Kr^+ {}^2P_{3/2}$ appears at the same photoelectron energy as the nonresonant five-photon ionization of Kr to $Kr^+ {}^2P_{1/2}$.

Examination of the PAD in terms of the coupling of the spin and orbital angular momenta helps us to understand how the photoelectrons are emitted. Since $M_J = 0$ is preserved, the magnetic quantum number of the total angular momentum j_e of the photoelectron in the $^2P_{1/2}$ channel is $m_{j_e} = -M_{J_C} = \mp 1/2$, where M_J and M_{J_C} are the magnetic quantum numbers of the total angular momenta J and J_C of Kr and Kr^+, respectively. For $m_{j_e} = \mp 1/2$, the possible combinations of (m_l, m_s) are $(0, \mp 1/2)$ and $(\mp 1, \pm 1/2)$, where m_s is the magnetic quantum number of the spin of the photoelectron. Considering a single active electron, the photoelectrons with even l orbitals of s,d, and g are preferred in the five-photon ionization from the outermost orbital of $4p$.

In the $^2P_{3/2}$ channel, $M_{J_C} = \pm 3/2$ is possible as well as $M_{J_C} = \pm 1/2$. When $M_{J_C} = \pm 3/2$, the possible combinations of (m_l, m_s) are $(\mp 1, \mp 1/2)$ and $(\mp 2, \pm 1/2)$. Therefore, only the $^2P_{3/2}$ channel is allowed to have the photoelectron orbitals with $m_l = 2$, irrespective of the presence of intermediate states. In the case of $l = 2$ and $m_l = \mp 2$, that is, the d_2 orbital, the photoelectrons are emitted toward the direction perpendicular to the laser polarization direction.

The remarkable intensity dependence of the perpendicular photoemission suggests the resonantly enhanced population transfer to specific Rydberg levels connecting to the d_2 photoelectron orbital. The autoionizing states are strong candidates of such Rydberg levels. In the experimental measurement, the autoionization to $^2P_{3/2}$ is expected to appear at the same energy as the nonresonant ionization to $^2P_{1/2}$.

From a theoretical point of view, it is difficult to simulate autoionization in the present TDDFT [56]. Additionally, stepwise ionization processes via a resonant intermediate state are not correctly included in the TDDFT. In order to numerically simulate the ionization from an electronically excited state, the potential of the electronically excited state of Kr is necessary. However, the present TDDFT has a limitation that only the potential of the electronic ground state is taken into account.

Nevertheless, we should examine resonant intermediate states below both ionization thresholds to $^2P_{3/2}$ and $^2P_{1/2}$. In the experiment at $I_0 = 8$ TW cm^{-2}, the substantial photoelectron yields in the range of $\theta = 45^\circ - 135^\circ$ exhibits nodes at $\theta = 75^\circ$ and 105° in the $^2P_{3/2}$ channel, suggesting that larger l photoelectron orbitals such as a g orbital ($l = 4$) emerge from an f-Rydberg state.

Considering the ponderomotive energy shift of Rydberg levels as well as ionization thresholds, resonant intermediate states should be located below the four-photon energy level in the field-free condition. In Fig. 5, the energy levels of Kr below the ionization thresholds for the formation of $Kr^+ {}^2P_{3/2}$ and $^2P_{1/2}$ are shown with the four- and five-photon energy from the electronic ground state ^1S of Kr. At $I_0 = 8$ TW cm^{-2}, the ponderomotive energy is $U_p = 0.118$ eV, represented by the thin arrow (a) in Fig. 5. Therefore, $6s$, $4d$, and $5p'$ are energetically allowed to be intermediate Rydberg states. In terms of the four-photon transition probability from the outermost $4p$ orbital in the electronic ground state of Kr ^1S, odd l orbitals such as p and f are preferred. As mentioned above, the PAD in the $^2P_{3/2}$ channel at $I_0 = 8$ TW cm^{-2} suggests the contribution of an f-Rydberg orbital to the intermediate state. However, there are no f orbitals below the four-photon energy. A possible explanation for the contribution of an f orbital is the dressed state formation of the $4d$ Rydberg levels and the highly lying f-Rydberg levels just below the ionization threshold for the formation of $Kr^+ {}^2P_{1/2}$. That is, the intermediate state is a dressed state, which is a linear combination of $4d$ and highly lying f-Rydberg states.

As I_0 increases from 8 to 18 TW cm^{-2}, the nodal structure of the PAD in the $^2P_{3/2}$ channel is suppressed. And then, as I_0 increases to 39 TW cm^{-2}, the number of the apparent nodes in the PAD decreases to two, suggesting that the contribution of a d orbital becomes dominant in photoemission.

The population in the autoionizing states such as $10s'$ is also explained by the dressed state formation as follows. The energy difference between $10s'$ and $5p$ levels is almost the same as the one-photon energy at $\lambda = 398$ nm, suggesting the

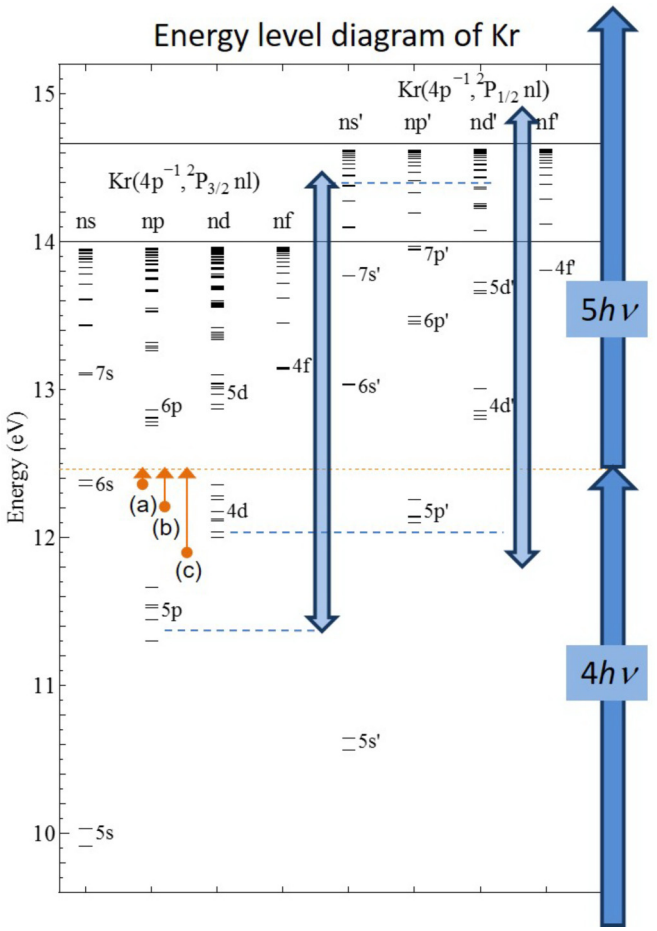

FIG. 5. Energy-level diagram of Kr converging to $^2P_{3/2}$ and $^2P_{1/2}$ of Kr^+ [50]. The energy on the left axis originates from the ground state ^1S of Kr. The length of the thick blue arrows corresponds to the one-photon energy of $\lambda = 398$ nm. The up arrows in the right side indicate the fourth and fifth photons required for the ionization from the electronic ground state of Kr. The double-headed arrows indicate the couplings between $5p$ and ns', and between $4d$ and nf, respectively, for the dressed state formation. The lengths of the thin yellow arrows labeled with (a), (b), and (c) indicate the ponderomotive energies of 0.118, 0.266, and 0.576 eV at $I_0 = 8$, 18, and 39 TW cm^{-2}, respectively.

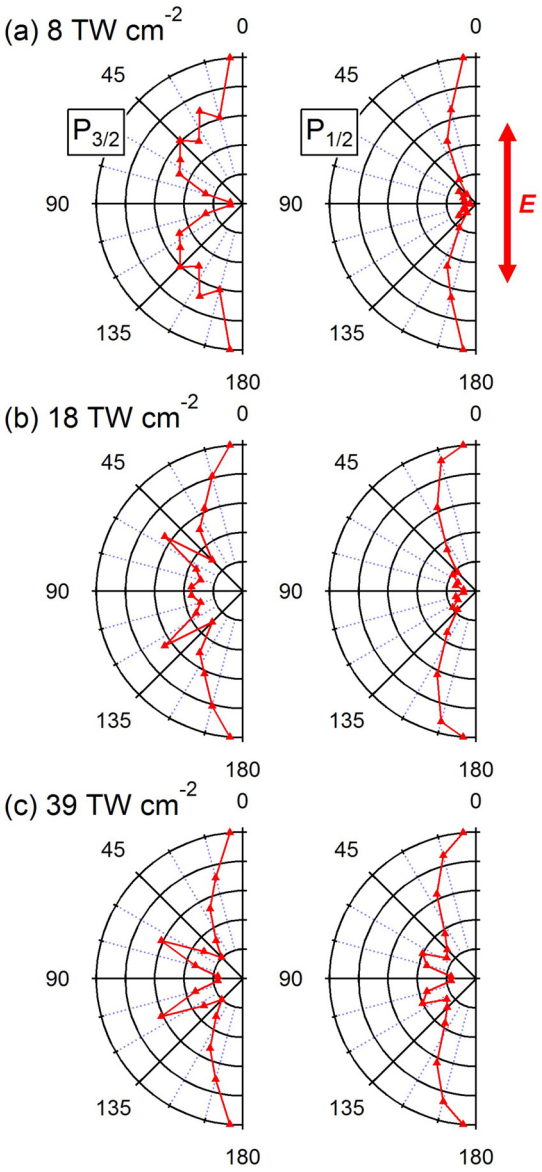

FIG. 6. Polar plots of measured photoelectron angular distributions of Kr to $^2P_{3/2}$ (left) and $^2P_{1/2}$ (right) through the six-photon ionization at the laser peak intensities I_0 = (a) 8, (b) 18, and (c) 39 TW cm^{-2}. The photon energy is 3.1 eV. The laser polarization direction is vertical.

strong dipole coupling for the dressed state formation as shown in Fig. 5. As I_0 increases to 39 TW cm^{-2}, the pondermotive energy shift causes four-photon near-resonant excitation to $5p$ Rydberg levels, with which the autoionizing states such as $10s'$ form the dressed states in the intense UV laser field. It is possible that population is nonadiabatically transferred to the upper level of the dressed states leading to the autoionization.

2. *Six-photon ATI*

In the photoelectron spectra shown in Fig. 2, the six-photon ATI is clearly separated from the five-photon ionization. The separation of the $^2P_{3/2}$ and $^2P_{1/2}$ channels in the six-photon ionization was based on the photoelectron energy in the same manner as the five-photon ionization. At $I_0 = 8$ TW cm^{-2}, the photoelectrons in the energy ranges of 4.29–4.87 eV and 3.57–4.09 eV were counted for the six-photon ionization channels to the formation of Kr^+ $^2P_{3/2}$ and $^2P_{1/2}$, respectively. As I_0 increases, each energy range was shifted by the ponderomotive energy. At $I_0 = 39$ TW cm^{-2}, the photoelectrons in the energy ranges of 3.85–4.39 eV and 2.93–3.47 eV were counted for the six-photon ionization channels to the formation of Kr^+ $^2P_{3/2}$ and $^2P_{1/2}$, respectively.

Polar plots of the measured PADs of the six-photon ATI are shown in Fig. 6. In the $^2P_{3/2}$ channel at $I_0 = 8$ TW cm^{-2}, the PAD exhibits five nodes, suggesting that larger l photoelectron orbitals such as an h orbital ($l = 5$) emerge through the two-photon transition from a dressed state containing an f state. As I_0 increases to 39 TW cm^{-2}, the photoelectron orbital in the $^2P_{3/2}$ channel becomes close to an f_0 orbital ($l = 3$, $m_l = 0$) with three nodes, as shown in Fig. 6(c). This trend is consistent with that of the five-photon ionization to $^2P_{3/2}$.

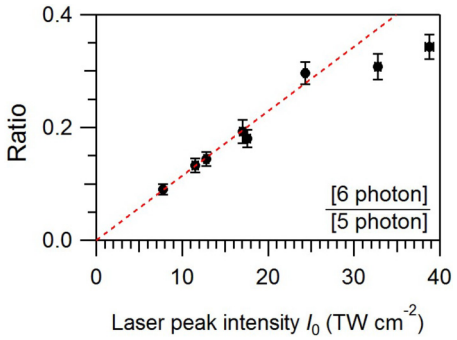

FIG. 7. Photoelectron yield ratio of the six-photon ATI with respect to the five-photon ionization (solid circle). A dashed straight line from the origin is the result of the least-squares fitting in the range of $I_0 < 25$ TW cm^{-2}. The errors of the yield ratios are obtained through propagation of errors. The errors of the counted event numbers of photoelectrons are assumed to be the square root of the counted numbers. The errors of the intensity are also obtained from the errors of the ponderomotive energy shift.

In the $^2P_{1/2}$ channel at $I_0 = 8$ and 18 TW cm^{-2}, the photoelectrons are dominantly emitted along the laser polarization, and a small photoelectron yield is measured in the range of $\theta = 45^\circ - 135^\circ$. As I_0 increases to 39 TW cm^{-2}, the photoelectron yield in the ranges of $\theta = 55^\circ - 85^\circ$ and $95^\circ - 125^\circ$ increases and the PAD becomes close to an f_0 orbital similar to the $^2P_{3/2}$ channel. This f_0 character in the six-photon ionization to $^2P_{1/2}$ is simply explained by the one-photon transition from a d_0 orbital at the five-photon level to a f_0-photoelectron orbital at the six-photon level. In the six-photon ionization, the photoemission yield toward $\theta = 90^\circ$ is much smaller than that toward $\theta = 0$ and 180°. This behavior is different from the five-photon ionization. In the autoionization, the photoelectron with a fixed energy is emitted from a bound Rydberg state through the configuration interaction. The autoionizing state is prepared through the five-photon absorption, while the additional one-photon excitation from the bound Rydberg state causes the direct ionization for the formation of $Kr^+ {}^2P_{1/2}$.

The photoelectron yield ratios of the six-photon ionization with respect to the five-photon ionization are plotted in Fig. 7. The areas of the peaks assigned to the five- and six-photon ionization in the measured photoelectron spectra in Fig. 2 are regarded as the respective yields. When I_0 is smaller than 25 TW cm^{-2}, the ratios as a function of I_0 are plotted on a straight line as shown in Fig. 7. This linear response of the ratio is consistent with the difference of one photon between the five- and six-photon processes.

At $I_0 > 30$ TW cm^{-2}, the lower energy side of the peak assigned to the five-photon ionization to $^2P_{1/2}$ is cut off at the photoelectron energy of 0 eV, as shown in Fig. 2(c). This means that the channel closing of the five-photon ionization partly takes place. However, the ratio of the six-photon ionization with respect to the five-photon ionization is suppressed from the straight line in the range of $I_0 > 30$ TW cm^{-2} as shown in Fig. 7. This suppression indicates the enhancement of the five-photon ionization and/or the reduction of the six-photon ionization. The enhancement of the five-photon ionization is consistent with the autoionization, because the autoionization takes place only in the five-photon ionization. The saturation of the six-photon ionization with respect to the five-photon ionization, and the increase in the yield of the seven-photon ionization alternative to the six-photon ionization, might also partly contribute to the suppression of the ratio.

V. SUMMARY

We have measured the 3D photoelectron momentum distributions of Kr in intense UV laser fields at the laser peak intensities I_0 in the range of 8–39 TW cm^{-2} and discussed the ionization routes on the basis of the PADs for the respective final ionic states of $^2P_{3/2}$ and $^2P_{1/2}$. As I_0 increases to 39 TW cm^{-2}, the photoemission toward the direction perpendicular to the laser polarization direction is anomalously enhanced in the five-photon ionization. This perpendicular photoemission is attributed to the autoionization to $^2P_{3/2}$, whose photoelectron energy coincides accidentally with that of the five-photon direct ionization to $^2P_{1/2}$. The theoretical calculation has been performed on the basis of the TDDFT including the spin-orbit interaction but has not reproduced the anomalous enhancement of the perpendicular photoemission. The disagreement between the experimental and theoretical results suggests the presence of resonant intermediate states including autoionizing states, because the TDDFT does not take account of the transient population at resonant intermediate states.

ACKNOWLEDGMENTS

The authors thank Prof. T. Nakajima (Kyoto University) for his valuable discussion. This study is partly supported by the Consortium for Photon Science and Technology programmed by MEXT of Japan. R.I. acknowledges JSPS KAKENHI (Grants No. 23350013 and No. 26288013) and the Joint Usage/Research Program on Zero-Emission Energy Research, Institute of Advanced Energy, Kyoto University (Grant No. ZE28B-7).

[1] S. L. Chin, C. Rolland, P. B. Corkum, and P. Kelly, Phys. Rev. Lett. **61**, 153 (1988).
[2] L. V. Keldysh, Zh. Eksp. Teor. Fiz. **47**, 1945 (1964) [Sov. Phys. JETP **20**, 1307 (1965)].
[3] F. H. M. Faisal, J. Phys. B: At. Mol. Phys. **6**, 584 (1973).
[4] H. R. Reiss, Phys. Rev. A **22**, 1786 (1980).
[5] A. Becker and F. H. M. Faisal, J. Phys. B: At., Mol. Opt. Phys. **38**, R1 (2005).
[6] P. Agostini, F. Fabre, G. Mainfray, G. Petite, and N. K. Rahman, Phys. Rev. Lett. **42**, 1127 (1979).
[7] R. R. Freeman, P. H. Bucksbaum, H. Milchberg, S. Darack, D. Schumacher, and M. E. Geusic, Phys. Rev. Lett. **59**, 1092 (1987).
[8] G. N. Gibson, R. R. Freeman, and T. J. McIlrath, Phys. Rev. Lett. **69**, 1904 (1992).
[9] H. Helm, N. Bjerre, M. J. Dyer, D. L. Huestis, and M. Saeed, Phys. Rev. Lett. **70**, 3221 (1993).

[10] V. Schyja, T. Lang, and H. Helm, Phys. Rev. A **57**, 3692 (1998).
[11] R. Wiehle, B. Witzel, H. Helm, and E. Cormier, Phys. Rev. A **67**, 063405 (2003).
[12] P. Kaminski, R. Wiehle, V. Renard, A. Kazmierczak, B. Lavorel, O. Faucher, and B. Witzel, Phys. Rev. A **70**, 053413 (2004).
[13] T. Marchenko, H. G. Muller, K. J. Schafer, and M. J. J. Vrakking, J. Phys. B: At., Mol. Opt. Phys. **43**, 185001 (2010).
[14] B. K. McFarland, J. P. Farrell, P. H. Bucksbaum, and M. Guhr, Science **322**, 1232 (2008).
[15] K. Hosaka, R. Itakura, K. Yokoyama, K. Yamanouchi, and A. Yokoyama, Chem. Phys. Lett. **475**, 19 (2009).
[16] H. Akagi, T. Otobe, A. Staudte, A. Shiner, F. Turner, R. Dorner, D. M. Villeneuve, and P. B. Corkum, Science **325**, 1364 (2009).
[17] O. Smirnova, Y. Mairesse, S. Patchkovskii, N. Dudovich, D. Villeneuve, P. Corkum, and M. Y. Ivanov, Nature (London) **460**, 972 (2009).
[18] M. Spanner and S. Patchkovskii, Phys. Rev. A **80**, 063411 (2009).
[19] E. Gubbini, U. Eichmann, M. Kalashnikov, and W. Sandner, Phys. Rev. Lett. **94**, 053602 (2005).
[20] L. Young, D. A. Arms, E. M. Dufresne, R. W. Dunford, D. L. Ederer, C. Höhr, E. P. Kanter, B. Krässig, E. C. Landahl, E. R. Peterson, J. Rudati, R. Santra, and S. H. Southworth, Phys. Rev. Lett. **97**, 083601 (2006).
[21] Z.-H. Loh, M. Khalil, R. E. Correa, R. Santra, C. Buth, and S. R. Leone, Phys. Rev. Lett. **98**, 143601 (2007).
[22] E. Goulielmakis, Z.-H. Loh, A. Wirth, R. Santra, N. Rohringer, V. S. Yakovlev, S. Zherebtsov, T. Pfeifer, A. M. Azzeer, M. F. Kling, S. R. Leone, and F. Krausz, Nature (London) **466**, 739 (2010).
[23] A. Fleischer, H. J. Wörner, L. Arissian, L. R. Liu, M. Meckel, A. Rippert, R. Dörner, D. M. Villeneuve, P. B. Corkum, and A. Staudte, Phys. Rev. Lett. **107**, 113003 (2011).
[24] L. Fechner, N. Camus, J. Ullrich, T. Pfeifer, and R. Moshammer, Phys. Rev. Lett. **112**, 213001 (2014).
[25] R. Santra, R. W. Dunford, and L. Young, Phys. Rev. A **74**, 043403 (2006).
[26] N. Rohringer and R. Santra, Phys. Rev. A **79**, 053402 (2009).
[27] H. J. Wörner and P. B. Corkum, J. Phys. B: At., Mol. Opt. Phys. **44**, 041001 (2011).
[28] R. Itakura, M. Fushitani, A. Hishikawa, and T. Sako, J. Phys. B: At., Mol. Opt. Phys. **47**, 195602 (2014).
[29] S. Lee, J. Lim, C. Y. Park, and J. Ahn, Opt. Express **19**, 2266 (2011).
[30] M. Goto and K. Hansen, Phys. Scr. **86**, 035303 (2012).
[31] W. D. M. Lunden, P. Sándor, T. C. Weinacht, and T. Rozgonyi, Phys. Rev. A **89**, 053403 (2014).
[32] P. Hockett, M. Wollenhaupt, C. Lux, and T. Baumert, Phys. Rev. Lett. **112**, 223001 (2014).
[33] M. Li, P. Zhang, S. Luo, Y. Zhou, Q. Zhang, P. Lan, and P. Lu, Phys. Rev. A **92**, 063404 (2015).
[34] L. Fechner, N. Camus, A. Krupp, J. Ullrich, T. Pfeifer, and R. Moshammer, Phys. Rev. A **92**, 051403(R) (2015).
[35] Z.-H. Loh, C. H. Greene, and S. R. Leone, Chem. Phys. **350**, 7 (2008).
[36] H. Wang, M. Chini, S. Chen, C.-H. Zhang, F. He, Y. Cheng, Y. Wu, U. Thumm, and Z. Chang, Phys. Rev. Lett. **105**, 143002 (2010).
[37] C. Ott, A. Kaldun, P. Raith, K. Meyer, M. Laux, J. Evers, C. H. Keitel, C. H. Greene, and T. Pfeifer, Science **340**, 716 (2013).
[38] C. Ott, A. Kaldun, L. Argenti, P. Raith, K. Meyer, M. Laux, Y. Zhang, A. Blättermann, S. Hagstotz, T. Ding, R. Heck, J. Madronero, F. Martin, and T. Pfeifer, Nature (London) **516**, 374 (2014).
[39] H. Mashiko, T. Yamaguchi, K. Oguri, A. Suda, and H. Gotoh, Nat. Commun. **5**, 5599 (2014).
[40] L. Argenti, A. Jiménez-Galán, C. Marante, C. Ott, T. Pfeifer, and F. Martín, Phys. Rev. A **91**, 061403 (2015).
[41] K. Hosaka, A. Yokoyama, K. Yamanouchi, and R. Itakura, J. Chem. Phys. **138**, 204301 (2013).
[42] T. Ikuta, K. Hosaka, H. Akagi, A. Yokoyama, K. Yamanouchi, F. Kannari, and R. Itakura, J. Phys. B: At., Mol. Opt. Phys. **44**, 191002 (2011).
[43] T. S. Clement, A. J. Taylor, and D. J. Kane, Opt. Lett. **20**, 70 (1995).
[44] E. Runge and E. K. U. Gross, Phys. Rev. Lett. **52**, 997 (1984).
[45] J. Kubler, K. H. Hock, J. Sticht, and A. R. Williams, J. Phys. F: Met. Phys. **18**, 469 (1988).
[46] R. G. Parr and W. T. Yang, *Density-Functional Theory of Atoms and Molecules* (Oxford University Press, New York, 1989).
[47] C. Hartwigsen, S. Goedecker, and J. Hutter, Phys. Rev. B **58**, 3641 (1998).
[48] K. Yabana and G. F. Bertsch, Phys. Rev. B **54**, 4484 (1996).
[49] T. Nakatsukasa and K. Yabana, J. Chem. Phys. **114**, 2550 (2001).
[50] E. B. Saloman, J. Phys. Chem. Ref. Data **36**, 215 (2007).
[51] X.-M. Tong and S.-I. Chu, Phys. Rev. A **64**, 013417 (2001).
[52] E. Mevel, P. Breger, R. Trainham, G. Petite, P. Agostini, A. Migus, J.-P. Chambaret, and A. Antonetti, Phys. Rev. Lett. **70**, 406 (1993).
[53] S. Chelkowski, T. Zuo, O. Atabek, and A. D. Bandrauk, Phys. Rev. A **52**, 2977 (1995).
[54] J. L. Dehmer, S. T. Pratt, and P. M. Dehmer, Phys. Rev. A **36**, 4494 (1987).
[55] Y. Morioka, M. Watanabe, T. Akahori, A. Yagishita, and M. Nakamura, J. Phys. B: At. Mol. Phys. **18**, 71 (1985).
[56] V. Kapoor, Phys. Rev. A **93**, 063408 (2016).